Space Weather

RESEARCH ARTICLE
10.1029/2024SW004112

Solar Wind and Magnetospheric Conditions for Satellite Anomalies Attributed to Shallow Internal Charging

J. V. Rodriguez[1,2], B. T. Kress[1,2], N. Y. Buzulukova[3,4,5], and R. J. Redmon[2]

[1]Cooperative Institute for Research in Environmental Sciences, University of Colorado, Boulder, CO, USA, [2]National Centers for Environmental Information, NOAA, Boulder, CO, USA, [3]Geospace Physics Laboratory, NASA Goddard Space Flight Center, Greenbelt, MD, USA, [4]Department of Astronomy, University of Maryland, College Park, MD, USA, [5]Partnership for Heliophysics and Space Environment Research (PHaSER), College Park, MD, USA

Abstract Satellite charging in Earth's magnetospheric plasma and radiation belts frequently causes operational anomalies. A recent study of a frequent Space Wire anomaly on GOES linked it to shallow internal charging by 100–300 keV electrons. Solar wind and magnetospheric conditions during a period spanning solar minimum (2017–2021) are analyzed to gain further insight into the anomalies. The anomalies are divided into two groups, with inter-anomaly intervals shorter than 2 days (clustered) and longer (background). The clusters sometimes exhibit a clear 27-day recurrence. The magnetic local time (MLT) distributions for background anomalies are statistically uniform, unlike those for clustered anomalies, which peak prior to local noon. The clustered anomaly distributions with respect to *Kp* are similar to those for surface charging, indicating enhanced plasma sheet access to geostationary orbit. The maximum 100–300 keV fluxes during injections are similar to published extreme fluxes. Through superposed epoch analysis and comparison with published lists of high-speed streams, clustered anomalies are determined to occur during high-speed streams with elevated solar wind speed, lower number density, and weakly negative interplanetary magnetic field B_z. The MLT and *Kp* dependencies of the clustered anomalies may indicate charge accumulating in a thin dielectric with a time constant less than 1 day. The background anomalies, occurring uniformly in local time and varying slowly between solar rotation periods, may indicate a distinct charging location with a time constant greater than a solar rotation.

Plain Language Summary Van Allen Belt electrons that deposit on satellite surfaces or penetrate inside satellites cause discharges that damage materials or send interfering radio bursts into electronics. Such damage and interference can cause satellite operational anomalies, for example, the famous case of the Galaxy 15 satellite which was out of control for 8 months following a charging event. Typically, electrons that cause these discharges have been accelerated through tens of thousands of volts or around a million volts before hitting the satellite. Electrons that have been accelerated to just over one hundred thousand volts have rarely been implicated in anomalies, until recently. Such electrons penetrate very thin shielding (about the thickness of a human hair) and accumulate until they discharge, causing interference in a data link. Clusters of anomalies recur approximately every 27 days, the rotational period of the Sun. Large increases in the number of electrons are needed to accumulate enough charge to cause a discharge. These increases can be traced back to periods of high speed (500 km per second and higher) solar wind that last several days and bring with them a fluctuating magnetic field that repeatedly transfers energy from the solar wind to the Van Allen Belt electrons.

Key Points:

- Space Wire anomalies are attributed to shallow internal charging by 100–300 keV electrons injected into GEO from the plasma sheet
- Solar wind drivers of these injections are high-speed solar wind streams with elevated speed, lower density and fluctuating magnetic field
- Anomaly variations in local time and across multiple solar rotations indicate two charging mechanisms with different time constants

Correspondence to:

R. J. Redmon and J. V. Rodriguez,
rob.redmon@noaa.gov;
juan.v.rodriguez@colorado.edu

Citation:

Rodriguez, J. V., Kress, B. T., Buzulukova, N. Y., & Redmon, R. J. (2025). Solar wind and magnetospheric conditions for satellite anomalies attributed to shallow internal charging. *Space Weather*, *23*, e2024SW004112. https://doi.org/10.1029/2024SW004112

Received 9 AUG 2024
Accepted 11 DEC 2024

Author Contributions:

Conceptualization: J. V. Rodriguez, R. J. Redmon
Data curation: J. V. Rodriguez
Formal analysis: J. V. Rodriguez, B. T. Kress
Funding acquisition: N. Y. Buzulukova, R. J. Redmon
Investigation: J. V. Rodriguez
Methodology: J. V. Rodriguez
Project administration: R. J. Redmon
Software: J. V. Rodriguez
Supervision: N. Y. Buzulukova
Validation: J. V. Rodriguez
Writing – original draft: J. V. Rodriguez
Writing – review & editing: J. V. Rodriguez, B. T. Kress, N. Y. Buzulukova, R. J. Redmon

1. Introduction

While the technological and societal effects of historically extreme solar events such as coronal mass ejections and energetic particle events rightly command attention because of their global impacts, the impacts of space weather are not limited to such extremes. There is a continuum of space weather storms between the extremes of benign ("breezes") and catastrophic ("hurricanes"), and it is important to improve our understanding of the middle ground of non-extreme geoeffective events and our ability to forecast and mitigate them (Schrijver, 2015). In aggregate, such non-extreme events form an important and underappreciated contribution to the overall social and economic effects of space weather. Satellite costs are increased through engineering, design and operations efforts to mitigate space weather effects and by loss of service due to anomalies (Green et al., 2017). Extreme solar events and large geomagnetic storms are not necessary for the occurrence of satellite anomalies. For example, an anomaly that caused a satellite to drift out of control while continuing to transmit, interfering with the operation of

other satellites in geostationary orbit, was associated with a locally extreme yet short-lived geomagnetic disturbance and plasma injection that took place during non-extreme solar activity and global geomagnetic disturbance levels (Loto'aniu et al., 2015). In general, satellite anomalies due to space weather are categorized as the effects of surface charging, internal charging, single-event effects, or total ionizing and displacement damage dose (O'Brien, 2009). This paper reports on the investigation of solar wind and magnetospheric conditions for a frequent non-destructive satellite anomaly attributed to internal spacecraft charging by electron fluxes at lower energies than are commonly associated with the phenomenon.

Surface charging results from the balance of currents from incident hot plasma electrons and ions, secondary electron and photoelectron emissions, and backscattered electrons (DeForest, 1972; Garrett, 1981). Surface charging in geosynchronous or geostationary orbit (GEO) is commonly caused by <50 keV electrons injected from the plasma sheet near midnight (DeForest, 1972; Matéo-Vélez et al., 2018; Mullen et al., 1986; NASA, 2017; Spence et al., 1993). The energy above which incident electron fluxes are not balanced by backscattered and secondary electron emission and therefore contribute to surface charging depends on spacecraft surface materials and configuration. Values of this lower energy have been observed in the range of 10 (Matéo-Vélez et al., 2018; Thomsen et al., 2013) to 30 keV (Mullen et al., 1986). The magnetic local time (MLT) distribution of anomalies or discharges due to surface charging in GEO is peaked between 21 and 6 MLT (Farthing et al., 1982; Koons et al., 2000; Wilkinson, 1994). The probabilities of observing a spacecraft frame potential <-100 V (Denton & Borovsky, 2012; Krause et al., 2000; Mullen et al., 1986; Thomsen et al., 2013) and differential charging levels <-100 V (Ozkul et al., 2001; O'Brien, 2009) in GEO follow a similar local time distribution. This local time distribution of surface charging and its effects closely follows the local time distribution of <50 keV electrons, which is determined by access of the plasmasheet to GEO near midnight, followed by eastward drift and rapid precipitation loss to the ionosphere, resulting in diffuse aurora in the morning sector (Korth et al., 1999; Thomsen et al., 1998). The occurrence of surface charging and associated anomalies in GEO is also correlated with the Kp index and reaches a peak at $Kp = 4$ to $Kp = 5$- or higher (Farthing et al., 1982; Garrett, 1981; Mullen et al., 1986; O'Brien, 2009; Spence et al., 1993; Thomsen et al., 2013).

Internal charging results from 100 to 3000 keV electrons penetrating shielding and accumulating in dielectrics or floating (ungrounded) conductors and poses a risk of a disruptive electrostatic discharge (ESD) if charge is deposited near vulnerable components (NASA, 2017; Spence et al., 1993). Unlike anomalies attributed to surface charging, those attributed to internal charging occur at all local times, sometimes with a fairly uniform distribution in MLT (Romero & Levy, 1993; Vampola, 1987). The accumulated charge depends on the internal charging current density, which depends on the incident flux and the shielding thickness, and on the electrical time constant of the charged material, which in vacuum can range from hours to as long as 2.8 years (Bodeau, 2010; Romero & Levy, 1993). Charge accumulation from penetrating electrons tends to reduce MLT dependence and to delay or reduce correlations with elevated geomagnetic disturbances (Lohmeyer & Cahoy, 2013). Following geomagnetic storms that result in their growth, elevated MeV electron fluxes can remain steady for up to 1 week under geomagnetically quiet conditions (Onsager et al., 2002). A correlation with multi-day fluences (or average fluxes) indicates that disruptive discharges follow days-long accumulation of charge. An occurrence of phantom commands attributed to internal charging based on a correlation with daily fluence of >2 MeV electrons observed by GOES-7 (Wrenn & Smith, 1996) led to the creation of a real-time alert issued by NOAA when GOES >2 MeV electron fluxes exceed a threshold. Balcewicz et al. (2000) found that certain anomalies on GEO communications satellites were well-correlated with high 7-day averages of >2 MeV electron fluxes. Failures of solid-state power amplifiers (SSPAs) in GEO attributed to internal charging occurred in all local time sectors, were independent of Kp, and were highly correlated with 14- and 21-day fluences of penetrating >2 MeV electron fluxes (Lohmeyer & Cahoy, 2013; Lohmeyer et al., 2015). In contrast, as observed on the Spacecraft Charging At High Altitude (SCATHA) satellite in a near-geosynchronous equatorial orbit, the MLT distribution of ESD pulses attributed to discharges from internal charging had a peak near noon (Fennell et al., 2001; Koons et al., 2000; Koons & Gorney, 1991) and was more likely to occur for $Kp > 4$ (Koons & Gorney, 1991). These discharges were associated with an increase in the flux of 288 keV electrons (Koons & Gorney, 1991). Cable charging was suggested as the source of SCATHA ESD pulses observed on the dayside following moderate substorms, when >300 and >1400 keV fluxes were highly elevated (Koons, 1983; Koons et al., 2000). These examples illustrate how the effects of internal charging can exhibit a range of correlations with environmental fluxes, local time and geomagnetic activity.

The existence of the NOAA >2 MeV electron alert has led to extensive work on the prediction of >2 MeV fluxes and their correlation with anomalies. The prominence of this alert has tended to obscure the importance to internal charging of the full electron energy spectrum and the actual shielding thickness (NASA, 2017), despite the public availability of GOES electron fluxes at more than one energy, starting with GOES-8 in 1995 (Onsager et al., 1996; Wrenn & Smith, 1996). Ferguson et al. (2011) determined that the Galaxy-15 anomaly was associated with a peak in 200–350 keV electron fluxes that were 4–5 times greater than the SCATHA "worst-case" electron flux spectrum (Fennell et al., 2001; Koons et al., 1988). Also, the >200 keV fluence over the 48 min prior to the anomaly exceeded the NASA (2017) threshold for internal discharging and could have affected thinly shielded, possibly ungrounded cables (Ferguson et al., 2011). However, surface charging could also have led to the Galaxy-15 anomaly (Ferguson et al., 2011; Loto'aniu et al., 2015). The ambiguous attribution was due in part to a lack of any radiation or charge monitors on Galaxy-15 and any electron measurements below 600 keV on the nearby GOES-11 spacecraft. Recently, using the full range (0.03–3,000 keV) of electron flux measurements from GOES-16 and -17 (Dichter et al., 2015), Kress et al. (2024) established that a frequent anomaly in a Space Wire command and telemetry channel on these satellites was most well associated with enhancements in 100 − 300 keV electron fluxes, and attributed this anomaly to shallow charging, to distinguish it from surface and internal charging. This anomaly, though occurring at all local times (LTs), was more likely to occur in the 6–12 LT sector on GOES-16, with a peak centered on 11 LT. The peak of this LT distribution was several hours later than the distribution of anomalies typically associated with surface charging reported in prior studies (Farthing et al., 1982; Koons et al., 2000; O'Brien, 2009; Wilkinson, 1994). The delay between the LT peak in 100 − 300 keV electron fluxes and the LT peak in the anomaly occurrence rate may have resulted from a charging/discharging time of 30 min to several hours, and/or local time dependence of conditions more favorable for ESDs. This evidence pointed to shallow internal charging, a term introduced by D. Pitchford to describe charge accumulation within thin non-conducting layers on satellite exteriors (D. Pitchford, private communication, 2019; Minow et al., 2024).

The present paper extends the work of Kress et al. (2024) to determine the variation in the anomaly occurrence rate over the study period (2017–2021) and its relationship to solar wind and magnetospheric conditions. Through superposed epoch analysis and by comparison with published lists of solar wind drivers, the dominant drivers of these anomalies are identified as high-speed streams from coronal holes. The fastest interplanetary coronal mass ejection (ICME) during the study period was much less effective in producing the anomalies than the preceding and following high-speed streams. This is likely due to the lack of quasi-periodic Alfvénic magnetic field variations (Belcher & Davis, 1971) in this ICME. The anomaly variations in local time and across multiple solar rotations provide evidence for two charging locations with different charge accumulation time constants. The association of the anomalies with injections established by Kress et al. (2024) is extended here by a correlation with *Kp*, a proxy for geomagnetic disturbance and enhanced plasma sheet access to GEO. The maximum 100–300 keV fluxes in these injections are shown to be consistent with published extreme fluxes.

2. Data

The radiation belt electron fluxes analyzed here are from the Magnetospheric Particle Sensor—High Energy (MPS-HI) flown on the GOES satellites that experienced the anomalies. During the study period, GOES-16 collected MPS-HI data at 89.5°W during 5 January–30 November 2017, then at 75.2°W starting 14 December 2017, while GOES-17 collected MPS-HI data at 89.5°W during 24 April–24 October 2018, then at 137.2°W starting 15 November 2018. Each MPS-HI consists of five electron telescopes and five proton telescopes arranged in a north-to-south fan, with the telescopes separated by 35° (Dichter et al., 2015). Each electron telescope records fluxes in 10 differential energy channels from 50 keV to 4 MeV (Boudouridis et al., 2020), covering the range of electron energies associated with internal charging. The GOES-16 and GOES-17 EXS_SPW anomaly data consist of lists of occurrence times (NOAA, 2024a). For a description of the anomaly, please see Kress et al. (2024). The GOES magnetic local times (MLTs) were accessed using the NASA Goddard Space Flight Center (GSFC) Satellite Situation Center Web (SSCWeb) service. These MLTs are calculated in the geomagnetic coordinate system (Russell, 1971) using the International Geomagnetic Reference Field (Alken et al., 2021), interpolated or extrapolated (after 2020) using day of year (T. Kovalick, private communication, 2024).

Both high-resolution and hourly averages of solar wind parameters are used in this work. The hourly solar wind parameters are from the OMNI hourly data set (King & Papitashvili, 2005; Papitashvili & King, 2020b). Solar wind data and geomagnetic indices used in superposed epoch analysis are taken from the OMNI 1-min data set (Papitashvili & King, 2020a). High-resolution solar wind data for individual cases are from the Wind Magnetic

Field Investigation (MFI) (Koval et al., 2021; Lepping et al., 1995) and the Solar Wind Experiment (SWE) nonlinear fits (Kasper et al., 2006; Ogilvie et al., 2021). The high-speed stream (HSS) catalog by Mariş Muntean et al. (n.d.); Besliu-Ionescu et al. (2022) and the list of near-earth interplanetary coronal mass ejections (ICMEs) compiled by Richardson and Cane (2010); Richardson and Cane (2024) are used to compare anomaly occurrence with the occurrence of these solar wind structures. The Bartels 27-day solar rotation periods (Bartels, 1934) are provided by the ACE Science Center (ASC, 2023). The 3-hr planetary *Kp* index (Matzka, Bronkalla, et al., 2021; Matzka, Stolle, et al., 2021) is analyzed for its association with the occurrence of the EXS_SPW anomaly.

3. Analysis

3.1. Anomaly Clusters

In order to identify common patterns in the EXS_SPW anomalies, associated radiation belt fluxes, and possible solar wind drivers, we plotted the GOES-16 EXS_SPW anomalies, MPS-HI 131 keV electron fluxes, and solar wind speed over 5 years (1 January 2017 to 31 December 2021) (Figure 1). We chose solar wind speed as a possible driver based on the pioneering correlation by Paulikas and Blake (1979) of enhancements in 0.14–3.9 MeV geosynchronous radiation belt fluxes with high-speed streams (HSS). In order to view individual anomalies clearly on this scale, they are dispersed vertically by plotting the inter-anomaly interval as the dependent variable on a logarithmic scale. The inter-anomaly interval is, for each anomaly, the interval from the previous anomaly. Remarkably, when plotted this way, the anomalies exhibit "clusters" in time with inter-anomaly intervals ranging over 3–4 orders of magnitude. These clusters sometimes exhibit clear 27-day periodicities, though their phasing with respect to the Bartels 27-day solar rotation periods (BRs) varies with time. This plot also reveals a fairly uniform background of anomalies occurring between the clusters that is characterized by inter-anomaly intervals longer than 1 day. The GOES-17 EXS_SPW anomalies and fluxes exhibited similar long-term behavior (not shown).

An example of one such anomaly "cluster" is shown in Figure 2. The inter-anomaly intervals of the EXS_SPW anomalies from GOES-16 and -17 are plotted over a period of 2 weeks (25 August–7 September 2020), along with 0.08–2.9 MeV electron fluxes observed by both satellites and the interplanetary magnetic field (IMF) and solar wind proton speed from Wind. The solar wind speed increases on 28 August to nearly 500 km/s, with a step change on 31 August to nearly 600 km/s. The IMF exhibits frequent quasi-periodic variations in B_z characteristic of Alfvén waves in high-speed streams (Belcher & Davis, 1971; Tsurutani et al., 2006). Particle injections (a signature of plasma sheet access to GEO (Korth et al., 1999; Nagai et al., 2019)) are frequent in the lowest energy channels and are absent only when IMF B_z is northward for a prolonged period (as on 3 September). The MeV fluxes grow substantially after the injections on 29 August and yet again after injections on 1 September. This growth could result from the acceleration to MeV energies of the injected seed population of 30–300 keV electrons by resonant interactions with chorus waves (e.g., Jaynes et al. (2015)) or slower (in comparison with injection time scale) radial diffusion in the presence of ULF waves (e.g., Loto'aniu et al. (2010)). Clusters of anomalies with inter-anomaly intervals less than 2 days are observed on GOES-16 and -17 on 31 August, with different anomaly times on the two spacecraft. A larger cluster of anomalies is observed on GOES-17 on 1 September with a large number of inter-anomaly intervals less than 1 hr. While it may be tempting to associate these anomalies with the growth in MeV electron fluxes, the high rate of anomalies does not continue beyond September 1 despite the persistence of high levels of MeV electron fluxes for several days, which is common radiation belt behavior in GEO after passage of a high-speed stream (Onsager et al., 2002).

3.2. MLT Distributions of Anomalies

The plot of inter-anomaly intervals shows a fairly uniform background of anomalies between anomaly clusters (Figure 1). This background is characterized by inter-anomaly intervals longer than an order of 1 day. In order to understand this behavior better, it is necessary to separate the local time distribution of this anomaly background from that of the anomaly clusters. Kress et al. (2024) showed that the local time distribution of GOES-16 EXS_SPW anomalies exhibited a peak before local noon and a minimum 2–4 hr before local midnight at which there was nonetheless a large number of anomalies.

Based on this observed behavior, we set a criterion of a 2-day inter-anomaly interval to distinguish background from clustered anomalies. This criterion will tend to group anomalies on consecutive days (Figure 2) within one cluster, which is a physically reasonable grouping, considering that geomagnetically disturbed periods can last

10.1029/2024SW004112

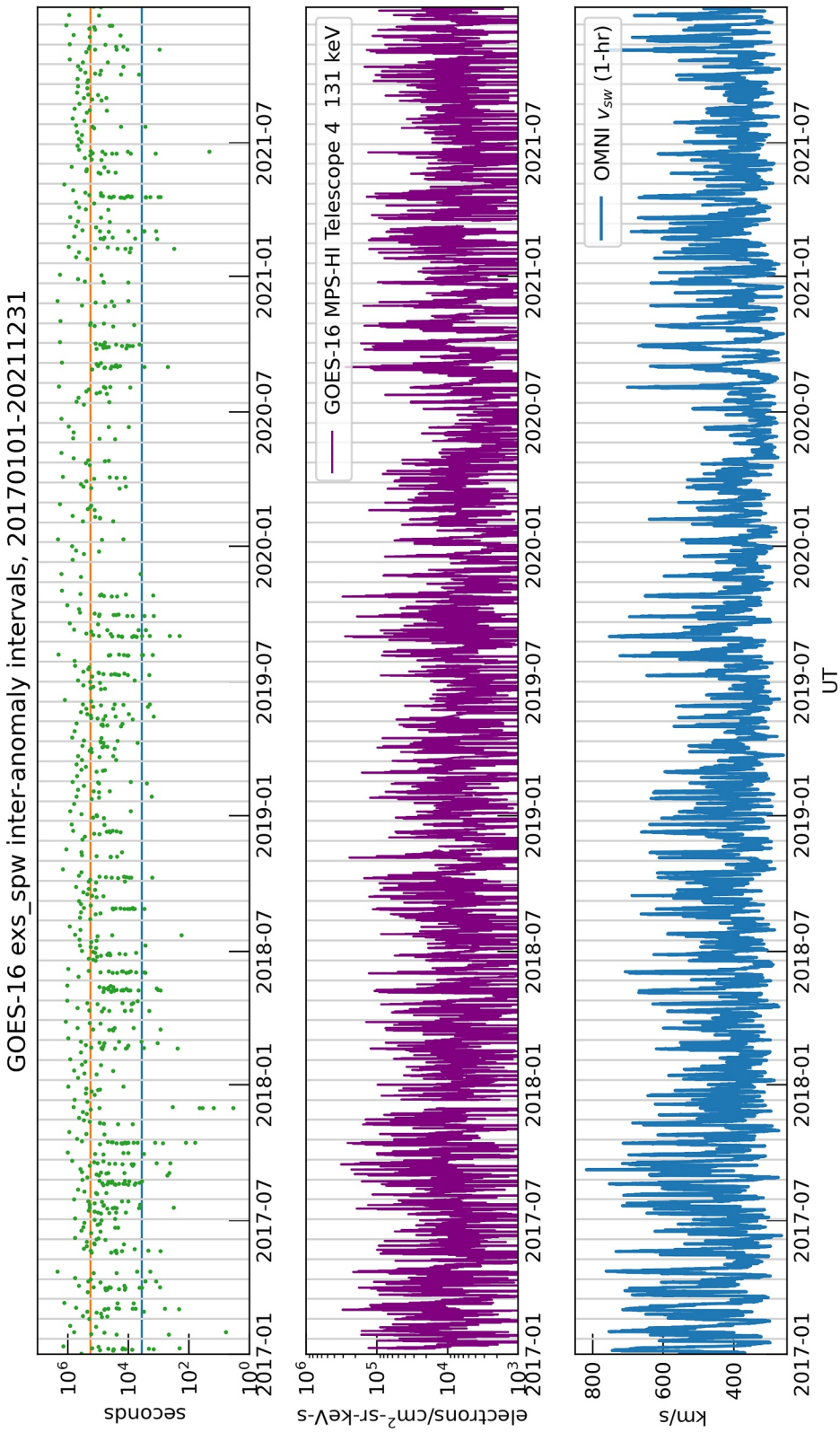

Figure 1. Synoptic comparison of GOES-16 EXS_SPW anomaly occurrences, radiation belt electron fluxes, and solar wind speed, January 2017 – December 2021. The beginning of each Bartels 27-day solar rotation period (BR) is indicated by a gray vertical line. Top panel: the anomaly occurrences are represented by the inter-anomaly intervals in seconds, on a logarithmic scale. At each point, the interval is between that anomaly and the prior anomaly. The blue horizontal line represents 1 hr and the orange line represents 2 days. Middle panel: GOES-16 MPS-HI 131 keV electron fluxes from telescope 4, subsampled to 1-hr cadence. Bottom panel: solar wind speed from the OMNI hourly data set.

10.1029/2024SW004112

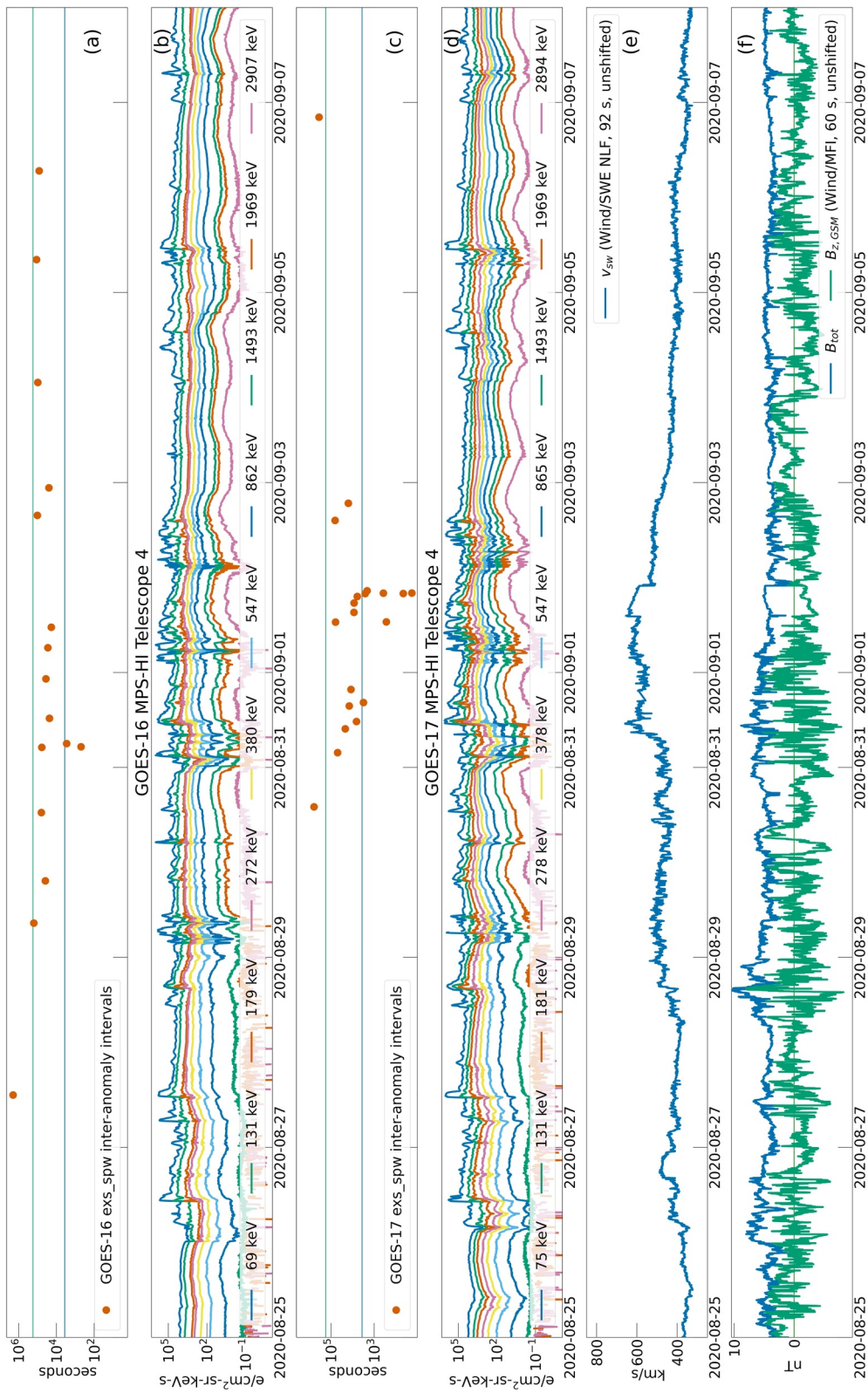

Figure 2. Example of clusters of EXS_SPW anomalies that occurred on GOES-16 and GOES-17 during the same series of particle injections during a high speed stream. (a) The GOES-16 anomaly occurrences are represented by the inter-anomaly intervals in seconds, on a logarithmic scale. At each point, the interval is between that anomaly and the prior anomaly. The blue horizontal line represents 1 hr and the green line represents 2 days. (b) Five-min averages of GOES-16 MPS-HI Telescope-4 electron differential fluxes, 0.08–2.9 MeV (The 2.0 and 2.9 MeV fluxes prior to August 30 are near instrument background levels.) (c) Like (a), for GOES-17. (d) Like (b), for GOES-17. (e) Solar wind velocity from the Wind Solar Wind Experiment (SWE) non-linear fits (Kasper et al., 2006). (f) Interplanetary magnetic field magnitude and Bz (GSM) from the Wind Magnetic Field Investigation (MFI). The time resolution of the Wind data is indicated on the plots.

longer than 1 day. However, it is still somewhat arbitrary and can result in ambiguities. For example, in Figure 2, the first GOES-17 anomaly (on 30 August 2020) follows an inter-anomaly interval of multiple days and is followed less than 1 day later by the next anomaly. Intuitively, the first anomaly appears to be part of the cluster. However, it is not part of the cluster if one applies the 2-day criterion to the preceding inter-anomaly interval only. On the other hand, if one applies the rule that an anomaly is part of a cluster if it is preceded or followed by an inter-anomaly period less than 2 days, then the anomaly on 30 August 2020 is included in the cluster. The combination of this rule and its logical inverse includes all anomalies. The inverse rule is that, if the inter-anomaly periods preceding and following an anomaly are greater than or equal to 2 days, then the anomaly is categorized as a background anomaly. The implications of this choice are interpreted in the Discussion section. We also note that the selection criterion is a free parameter which, chosen appropriately, should demonstrate a clear difference in the statistical characteristics of two anomaly populations.

To evaluate the null hypothesis that an observed distribution is drawn from a distribution that is uniform in magnetic local time (MLT), we calculate the chi-square probability function $Q(\chi^2|\nu)$. The chi-square statistic for the anomaly MLT distributions is given by (Press et al., 1988)

$$\chi^2 = \sum_i \frac{(N_i - n_i)^2}{n_i} \tag{1}$$

where, in the ith MLT bin, N_i is the number of observed anomalies and n_i is the expected number of anomalies for a uniform distribution. The sum of $\{n_i\}$ is set equal to the sum of $\{N_i\}$. This reduction in the degrees of freedom reduces ν by one from the number of MLT bins (e.g., from 12 to 11). $Q(\chi^2|\nu)$, a regularized upper incomplete gamma function, is the probability that the sum of the squares of ν random variables is greater than χ^2 (Press et al., 1988). The larger the value of Q, the more likely the null hypothesis is true and the observed distribution is drawn from a uniform distribution. Q is 1 at $\chi^2 = 0$ and 0 at large χ^2 and is a steep function of χ^2/ν in the vicinity of $\chi^2/\nu = 1$.

The resulting MLT distributions are shown in Figure 3 for both satellites. A pre-noon peak is evident in the GOES-16 and -17 clustered distributions (as is the case for all anomalies (Kress et al., 2024)). The background distributions are statistically much more uniform in MLT than the clustered anomalies: for the clustered distributions, Q was of order 10^{-10} for GOES-16 and 10^{-15} for GOES-17, while for the background distributions, Q is 0.67 for GOES-16 and 0.094 for GOES-17. This result shows that the separation of the anomalies into clustered and background groups using a criterion based on the inter-anomaly interval provides a useful framework for gaining further insight into their behavior and possible causes.

3.3. *Kp* Distributions of Anomalies

Surface charging is commonly correlated with the 3-hr *Kp* index (Farthing et al., 1982; Garrett, 1981; O'Brien, 2009; Spence et al., 1993; Thomsen et al., 2013), and internal charging is occasionally (Koons & Gorney, 1991) though not always (Lohmeyer & Cahoy, 2013) correlated with *Kp*. Therefore, the association of the EXS_SPW anomalies with *Kp* is of interest. The distributions of *Kp* at the times of GOES-16 and -17 EXS_SPW anomalies from the first day of MPS-HI data through December 2021 are shown in Figure 4, normalized to the total occurrence of each 3-hr *Kp* index value during this period, and separated into the distributions for the clustered and background anomalies. Multiple anomalies within the same 3-hr period contribute to the histograms. This reflects the fact that the EXS_SPW anomalies sometimes occur in rapid succession (On GOES-17, there were 7 clustered anomalies in the single 3-hr period for which *Kp* was equal to 8-; the histogram is clipped to 1 anomaly per index period.) The probability of the occurrence of the EXS_SPW clustered anomalies clearly increases with *Kp*, up to *Kp* = 6- for GOES-16 (10 occurrences) and 5+ for GOES-17 (11 occurrences), above which the statistics are poor during the study period. In contrast, the probability of the occurrence of the EXS_SPW background anomalies is uniform (The spike in the GOES-16 distribution at *Kp* = 6+ represents a single anomaly.) The *Kp* index is sensitive to the strength of the magnetospheric convection electric field, which affects the location of the inner edge of the plasma sheet and the access of plasma sheet populations to GEO (Korth et al., 1999; Thomsen, 2004). Therefore, this correlation with Kp indicates that the EXS_SPW clustered anomalies are associated with recent (perhaps within 3 hr) access of plasma sheet populations to GEO.

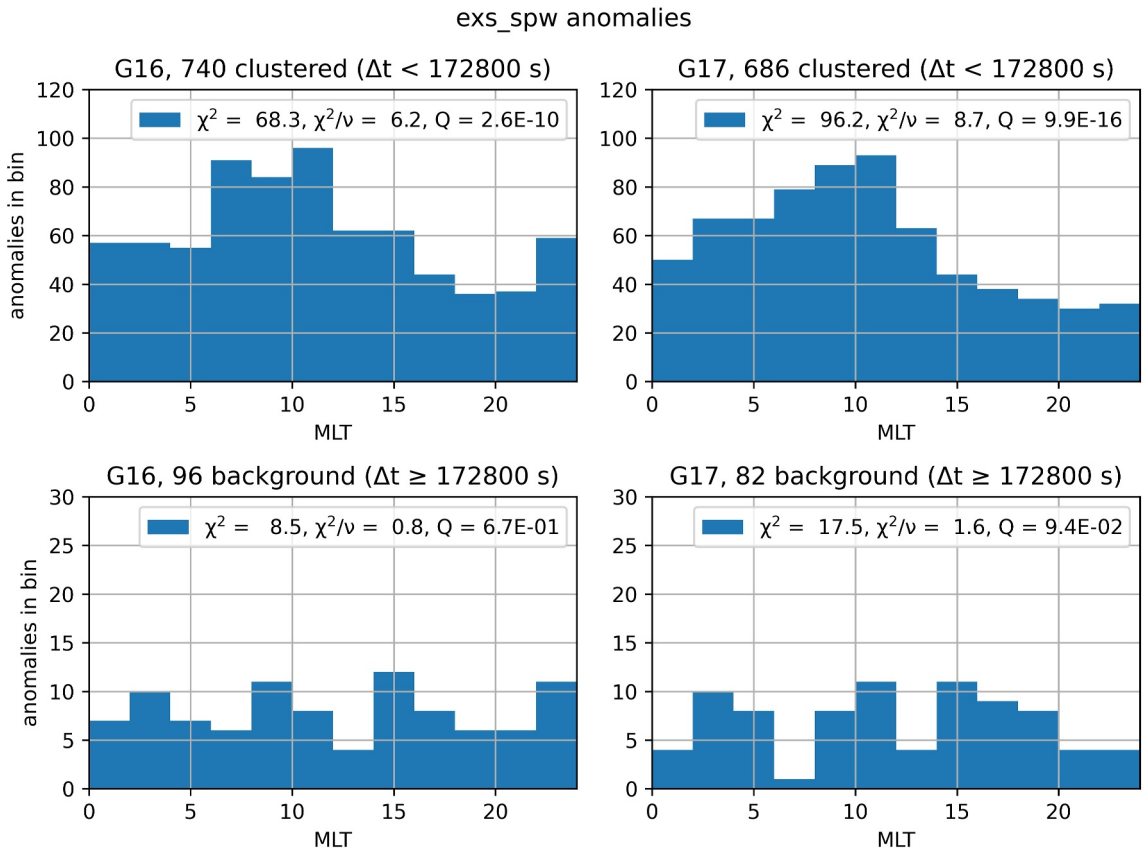

Figure 3. Magnetic local time (MLT) distributions of the GOES-16 and -17 EXS_SPW anomalies, separated into clustered (upper row) and background (lower row) anomalies. The inter-anomaly interval criterion for separating background and clustered anomalies is 2 days. On each plot are the values for χ^2, χ^2/ν, and Q resulting from the null hypothesis that the distributions are drawn from a uniform distribution in MLT.

3.4. Anomalies by Solar Rotation Period

To quantify the time variation of the EXS_SPW anomalies over several years (the study period), we plot the total number of anomalies by Bartels solar rotation period (BR), separating them into clustered and background anomalies as determined in Section 3.2. The results are shown in Figure 5 for both satellites. The number of anomalies with inter-anomaly intervals longer than 2 days varies slowly about the mean of 1.3 anomalies per BR. In contrast, the number of anomalies with shorter inter-anomaly intervals varies greatly from BR to BR, from zero to a maximum of 25 for GOES-16 and 36 for GOES-17. The inter-anomaly intervals depend at a minimum on the internal charging current density and the electrical time constant of the charged material. Short intervals suggest high charging currents and a short time constant causing the breakdown potential to be reached rapidly. Thus the clustered anomalies may be traced to a susceptibility to a high-flux (100–300 keV) population that varies from one BR to the next—a susceptibility that may have a short time constant. In contrast, the population driving the background anomalies is fairly constant from one BR to the next and less intense than that driving the clustered anomalies, or the time constant of the susceptibility has a time constant longer than a BR.

3.5. Superposed Epoch Analysis of Solar Wind Drivers and Geomagnetic Indices

Figure 1 showed that EXS_SPW anomaly clusters were sometimes clearly associated with peaks in solar wind speed. In this section, superposed epoch analysis (SEA) is used to determine the range of several solar wind drivers and geomagnetic indices associated with these anomalies and to identify any changes at the times of the anomalies. Like Kress et al. (2024), who performed SEA on 30 eV–2 MeV electron fluxes observed by GOES-16, each epoch comprises 12 hr prior to and 12 hr following each anomaly. The SEA is performed separately for the clustered and background anomalies. The quantities analyzed include the IMF field components in geocentric solar magnetospheric (GSM) coordinates, solar wind speed v_{sw} and number density n_{sw}, and the 1-min SYM-H

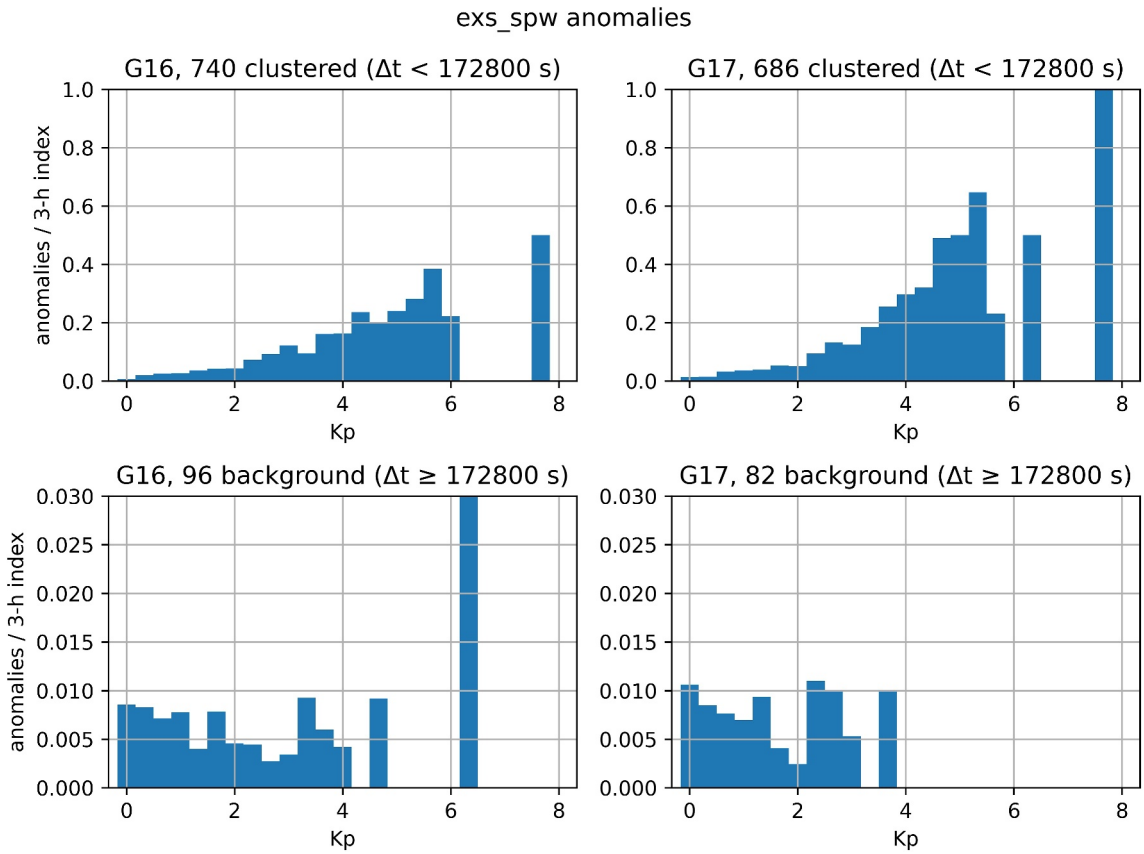

Figure 4. *Kp* distributions of the GOES-16 and -17 EXS_SPW anomalies, separated into clustered (upper row) and background (lower row) anomalies. The inter-anomaly interval criterion for separating background and clustered anomalies is 2 days. Each bin contains the average number of EXS_SPW anomalies per 3-hr *Kp* index during the study period, for GOES-16 and -17. The statistics are poor (fewer than 10 samples) above $Kp = 6-$ (GOES-16) and 5+ (GOES-17) for the clustered anomalies, and above $Kp = 2-$ (GOES-16) and 1+ (GOES-17) for the background anomalies.

and auroral electrojet (*AE*) family of geomagnetic indices. The source of these data is the 1-min OMNI data (Papitashvili & King, 2020a). The SYM-H and the *AE* indices are measures, respectively, of the geomagnetic storm strength and the global auroral electrojet activity associated with these anomalies (Baumjohann, 1986). For reference, the GOES-16 131 keV electron fluxes, the energy most enhanced in association with the anomalies (Kress et al., 2024), are also analyzed. The analysis is restricted to 2017–2019 since the *AE* indices were not available beyond December 2019 when the analysis was performed. However, the results of the SEA of the other quantities for the longer period (2017–2021) are similar.

The results of the SEA of IMF B_z, solar wind speed and density, SYM-H, *AL*, and the GOES-16 131 keV electron fluxes are shown in Figure 6. The mean B_z was slightly negative (>-1 nT) prior to the clustered anomalies and approached zero thereafter. The mean values of IMF B_x and B_y (not shown) were close to zero throughout the epochs. For the clustered anomalies, v_{sw} was elevated ($\sim$550 km/s) and decreasing slightly, while for the background anomalies it was much lower ($\sim$400 km/s). In contrast, n_{sw} was somewhat greater for the background ($\sim 6 - 7$ cm^{-3}) than for the clustered anomalies ($\sim$5 cm^{-3}, decreasing slightly throughout the epoch). SYM-H varied little, with the mean being ~ -19 nT for the clustered anomalies and ~ -7 nT for the background anomalies. A drop in the magnitude of the lower quartile of SYM-H at the time of the clustered anomalies is evident. The *AL* index (and the *AE* and *AU* indices, not shown) exhibit a marked decrease in magnitude starting $\sim$1 hr before the time of the clustered anomalies ($\sim$50 nT in 2 hr in the mean). No such decrease is observed at the time of the background anomalies. The electrojet indices are also more elevated in the mean for the clustered anomalies ($\sim$200 nT) than for the background anomalies. The peak in the mean 131 keV fluxes shown here for the clustered anomalies is similar to that derived by Kress et al. (2024) for all anomalies, and a similar peak is evident in the upper quartile. In contrast, there is no peak in the upper quartile of the fluxes associated with the background

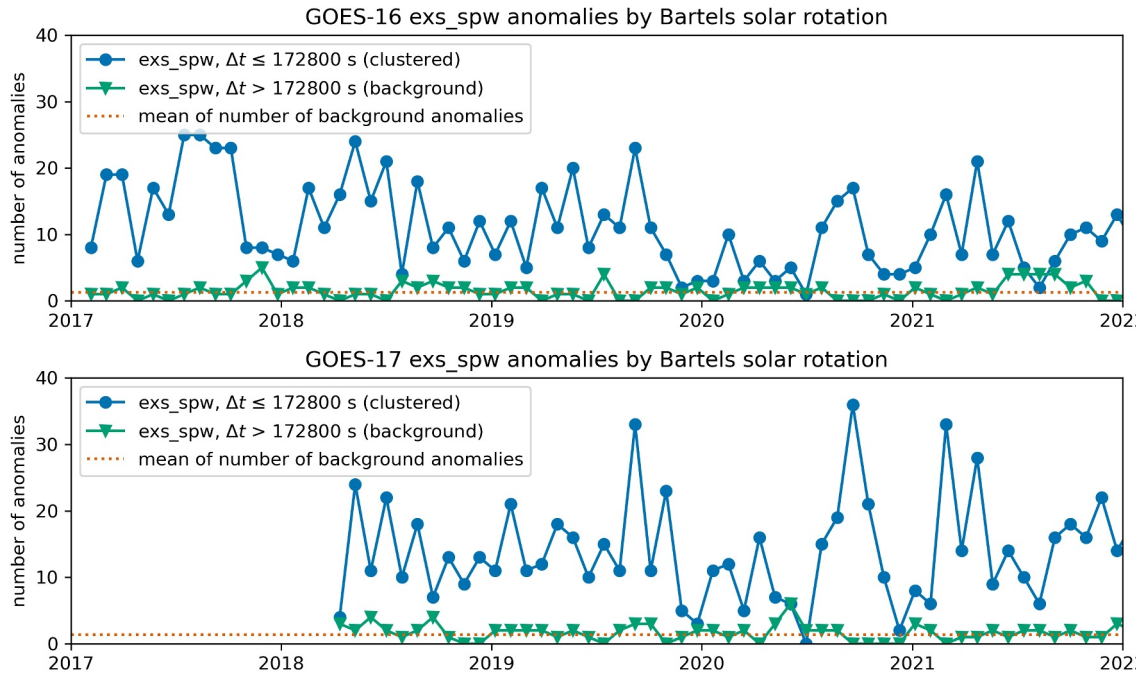

Figure 5. Number of GOES-16 (top) and −17 (bottom) EXS_SPW anomalies per Bartels solar rotation period (BR). The GOES-16 time series corresponds to the top panel of Figure 1. The anomalies are separated into those with inter-anomaly intervals (relative to the previous anomaly) less than 2 days (clustered) and greater than 2 days (backgrounds). The dotted line indicates the mean of the number of background anomalies per BR, which is approximately 1.3.

anomalies, and a weak peak in the mean just prior to the zero epoch is comparable to one observed 4 hr after the anomaly.

Under the conditions of Alfvénic fluctuations in high-speed streams, the IMF needs a significant southward offset to result in the largest flux enhancements in GEO (Miyoshi & Kataoka, 2008). However, the change in B_z around the time of the injections suggests that a negatively biased B_z is not always a sufficient condition for the injections. Northward turnings of B_z, known to trigger substorms (Hsu & McPherron, 2003; Lee et al., 2006), could be influencing the statistics here. The elevated v_{sw} associated with clustered anomalies is consistent with their occurrence during HSS, as is the lower (but not extremely low) n_{sw}, which drops upstream of a stream interface (Burlaga, 1974). The value of B_z is similar for clustered and background anomalies. However, the slight increase (approach to zero) starting ∼2 hr before the anomaly is more clear for the clustered anomalies. It is seen in the mean as well as the median and upper and lower quartiles.

Stream interaction regions and resulting outer belt electron flux increases are known to be associated with weak geomagnetic activity levels (Miyoshi & Kataoka, 2008; Tsurutani et al., 2006). The SYM-H results show that greater mid-latitude geomagnetic activity (though still weak) is associated more with the clustered anomalies than the background anomalies. *AL* and *AU* are sensitive to the strength of the westward and eastward electrojets, respectively, and *AE* is their difference. The results indicate that the strengths of the westward electrojet and of the eastward electrojet increase starting about 3 hr before the anomaly (observed as a dip in *AL*), then decrease starting about an hour prior to the clustered anomalies (but not the background anomalies). There is no such dip in SYM-H at the 25th percentile, but it does increase at the same time as *AL*, consistent with the fact that the mid-latitude geomagnetic disturbance indices are affected by field-aligned currents and electrojets (Baumjohann, 1986; Weygand & McPherron, 2006). Similar changes in the electrojet indices are observed in SEA based on the GOES-17 anomaly times (not shown). Though not entirely independent assessments, the similar behavior of the electrojet indices associated with the GOES-16 and -17 anomalies indicates that the observed change is not a quirk of the specific anomaly times used, since they differ between the two spacecraft (e.g., Figure 2). The observed changes in the indices, which run counter to the expected increase in magnitude at substorm onset (McPherron & Manka, 1985), may originate from large field-aligned currents which in these cases on average partially cancel the fields from the horizontal electrojet (Baumjohann, 1986). Interestingly, the AL dip preceding

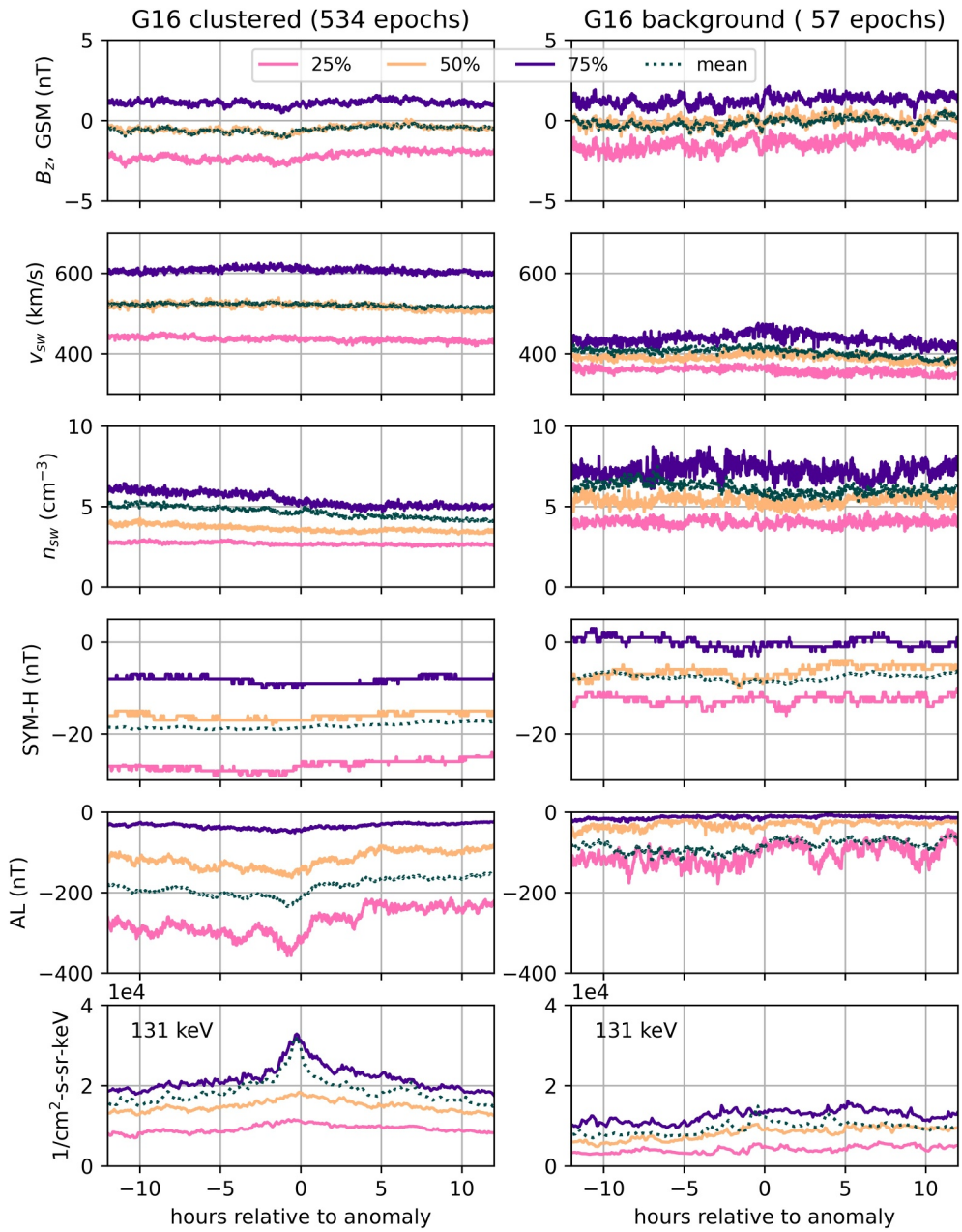

Figure 6. Superposed epoch analysis of OMNI 1-min solar wind quantities (B_z GSM, v_{sw}, n_{sw}), geomagnetic indices (SYM-H, *AL*), and GOES-16 131 keV electron fluxes, 2017–2019, for (left) clustered anomalies and (right) background anomalies. Results are represented by the mean (dotted line), median and upper and lower quartiles (Denton & Borovsky, 2012).

the anomaly lasts ∼3 hr, a typical substorm duration time. A close look reveals a delay between substorm expansion (minimum in *AL*) and the peak of 131 keV fluxes at GEO, and a subsequent delay between the peak flux and the anomaly time, both ∼30 min, also noted by Kress et al. (2024). We leave the analysis of these fine-structured details for future studies. However, it is noteworthy that the minima in *AL* at the time of worst-case electron spectra for surface charging (Ganushkina et al., 2021) are much sharper than the AL minimum observed ∼30 min before the peak flux and ∼60 min before the anomaly in Figure 6. The minima exhibited by IMF B_z ∼1–1.5 hr prior to the occurrence of these severe spectra (Ganushkina et al., 2021) are also much deeper than those evident in Figure 6 at a similar time prior to the EXS_SPW anomaly. These comparisons show that solar wind and magnetospheric conditions associated with worst-case electron spectra for surface charging are distinct from those associated with the EXS_SPW anomaly.

Table 1
Statistics of HSS and EXS_SPW Anomaly Occurrence

Statistic	GOES-16	GOES-17
Number of HSS during MPS-HI observations through 2019	117	67
Number of anomalies through 2019	617	374
Fraction HSS with clustered anomalies	0.63	0.67
Fraction HSS with background anomalies	0.27	0.22
Fraction clustered anomalies during HSS	0.83	0.91
Fraction background anomalies during HSS	0.58	0.44
Fraction total period during HSS	0.54	0.54
Median HSS peak velocity with anomalies (km/s)	590	550
Median HSS peak velocity w/o anomalies (km/s)	475	472
Median HSS max. velocity change with anomalies (km/s)	251	216
Median HSS max. velocity change w/o anomalies (km/s)	133	121

3.6. Statistical Association With HSS

The SEA results show that, at the mean, median and upper quartile, the clustered anomalies are associated with solar wind velocities characteristic of high-speed streams (HSS), but this is not necessarily the case at the lower quartile. Therefore, in order to determine a clearer statistical association between the anomalies and HSS, we use the catalog of HSS during solar cycle 24 derived by Mariş Muntean et al. (n.d.) using the method of Besliu-Ionescu et al. (2022). This list ends in 2019 and thus covers only a 3-year portion of the study period (2017–2019). Nonetheless, there were 117 HSS during the GOES-16 observations and 67 during the GOES-17 observations through December 2019, permitting adequate statistics. For this catalog, a HSS is defined as a solar wind flow having a 1-day jump in speed of >100 km/s (between the minimum 3-hr average on 1 day and the maximum 3-hr average on the following day) (Besliu-Ionescu et al., 2022; Lindblad & Lundstedt, 1981). The start of the event is identified as the start of this jump, and the end of the event is identified when the speed returns to the value at the start of the initial jump. A subsequent >100 km/s increase during an ongoing HSS is identified as the start of a new HSS and the end of the ongoing HSS. Only HSS associated with coronal holes are included in the catalog. For more details please see Besliu-Ionescu et al. (2022).

We compared this catalog of HSS with the list of GOES-16 and -17 EXS_SPW anomalies to determine the following statistics: the fraction of the anomalies that occurred during HSS, the fraction of HSS during which anomalies occurred, and the difference in the statistics between the clustered and background groups of anomalies. The results are summarized in Table 1. The similarity of the results between the two spacecraft indicates similar susceptibilities to the environment. The salient result is that the fraction of clustered anomalies during HSS was much greater (0.83 for GOES-16, 0.91 for GOES-17) than the fraction of time occupied by HSS (0.54), which indicates that HSS strongly drive the clustered anomalies. The fraction of background anomalies during HSS (0.44–0.58) bracketed the fraction of time occupied by HSS (0.54), which suggests the lack of a significant association between HSS and background anomalies. The converse statistic showed that not all HSS were associated with anomalies (0.63–0.67 were associated with clustered anomalies, 0.22–0.27 were associated with background anomalies). HSS associated with anomalies had greater median peak speeds and greater median increases in speed from the onset to the peak of the HSS.

3.7. Relative Effectiveness of HSSs and ICMEs

In the Richardson and Cane (2024) catalog of interplanetary coronal mass ejections (ICMEs) (Richardson & Cane, 2010), only 24 ICMEs occurred during 2017–2019. Furthermore, comparison with the HSS catalog of Mariş Muntean et al. (n.d.) determines that 12 of these ICMEs overlapped with HSS originating in coronal holes, making their effects difficult to disentangle. Such a low number of ICMEs, expected at the end of a solar cycle, precludes a statistical comparison of the effectiveness of HSS and ICMEs in driving the particle injections which lead to the EXS_SPW anomalies. However, an evaluation of the effectiveness of the ICME associated with the greatest solar wind speed v_{sw} observed during the study period is instructive.

From the nonlinear fits to the Wind/SWE observations (Ogilvie et al., 2021), the highest v_{sw} was 847 km/s at 0737 UT on 8 September 2017, during BR2511, a period of highly geoeffective space weather (Redmon et al., 2018). In addition to four X-class flares and two large solar energetic particle events, which we do not discuss further, there were two HSS and three ICMEs during this BR (Figure 7). We adapt the nomenclature of Redmon et al. (2018) for the HSS and ICMEs observed during this period. The highest v_{sw} and the largest negative IMF B_z values were observed during ICME1. However, only three anomalies were observed during ICMEs, one during ICME1 on 8 September and two during ICME2 on 13 September. In contrast, two anomaly clusters were observed during HSS0 (30 August–4 September) and HSS1 (15–20 September) comprising 20 anomalies. The behavior of the IMF during ICME1 is key to understanding the difference. A large southward turning of B_z shortly before 12 UT on 8 September resulted in a large injection observed by GOES-16, followed by several drift echoes (and one EXS_SPW anomaly). However, after the southward turning, the IMF vector rotated rather rapidly such that by 00 UT on 9 September, B_z was near zero and the IMF was radial (B_x dominant). The resulting reduction in convection cut off plasma sheet access to GEO, and with only loss processes operating, fluxes below 300 keV decayed for the rest of ICME1. Such radial IMFs are observed in the trailing region of approximately one-fifth of ICMEs (Neugebauer et al., 1997). Therefore, while not unusual, this behavior in ICME magnetic fields is not dominant. In contrast, both HSSs were characterized by continual fluctuations in the B_z component, resulting in multiple injections, as is commonly observed during HSS (Lee et al., 2006). This comparison shows that the fluctuating, low-amplitude IMF during HSS can be more effective in driving the injections that cause the EXS_SPW anomalies than the dramatic, large IMF in shocks and CMEs.

4. Discussion

Thomsen et al. (2013) identified three characteristics of a spacecraft anomaly that can be used to identify a probable environmental cause: "(1) statistically significant association with the presence of a particular population…; (2) statistically significant association with elevated magnetospheric activity, typically *Kp*…; and (3) a nonuniform occurrence distribution in local time…" The EXS_SPW anomaly has been characterized in these three ways by Kress et al. (2024) and in the present paper. Using three statistical methods, Kress et al. (2024) determined the first characteristic, namely that 100–300 keV fluxes were most elevated in association with this anomaly. Thomsen et al. (2013) pointed out that (1) may be difficult to determine in the case of internal charging if the accumulation period is long. While this is commonly the case with internal charging, it does not present a problem in the present case since the electrical time constant of the charged dielectric appears to be short (<1 day). Regarding (2), the anomaly was shown to be associated with elevated *Kp* in Section 3.3 of this paper. This indicates a magnetospheric origin for the causative population but is otherwise ambiguous (Thomsen et al., 2013); indeed, surface charging is well known to be associated with elevated *Kp*. This ambiguity and the shallow penetration depth of this population (0.0076 cm in aluminum for 131 keV electrons, which is 78 times the penetration depth for 10 keV electrons (Tabata et al., 1972)) might lead to the conclusion that this is still surface charging, if other characteristics of the anomaly are not considered.

Thomsen et al. (2013) considered (3) to be more definitive since different populations have different local time (LT) distributions. Kress et al. (2024) showed that this anomaly occurred at all LTs and was still more likely to occur in the 6–12 LT sector, where fluxes above 100 keV have their maximum in LT (Ganushkina et al., 2019; Kress et al., 2024), with a peak centered on 11 LT, about 4 hr later than the 131 keV flux peak (Kress et al., 2024). The LT peak and significant uniform background of the EXS_SPW anomaly are quite distinct from the LT distribution of surface charging, which reflects that of 10–50 keV electrons above some flux threshold. Further analysis in Section 3.2 of this paper shows that the EXS_SPW anomalies can be separated into clustered and background groups, which have, respectively, distributions that are peaked pre-noon and uniform in LT. Taken together, these three statistical characteristics clearly indicate an anomaly caused by magnetospheric populations that are distinct from the 10 to 50 keV electrons associated with surface charging. This phenomenon deserves a distinct name; we have used "shallow internal charging."

4.1. Implications for Charging Mechanism

The periods during HSS when the clustered anomalies are observed are characterized by numerous electron injections from the plasma sheet into geostationary orbit (Figures 2 and 7). This is consistent with a *Kp* correlation similar to that previously reported for surface charging that indicates improved access of plasma sheet populations to GEO due to enhanced magnetospheric convection (Farthing et al., 1982; Garrett, 1981; O'Brien, 2009; Spence

10.1029/2024SW004112

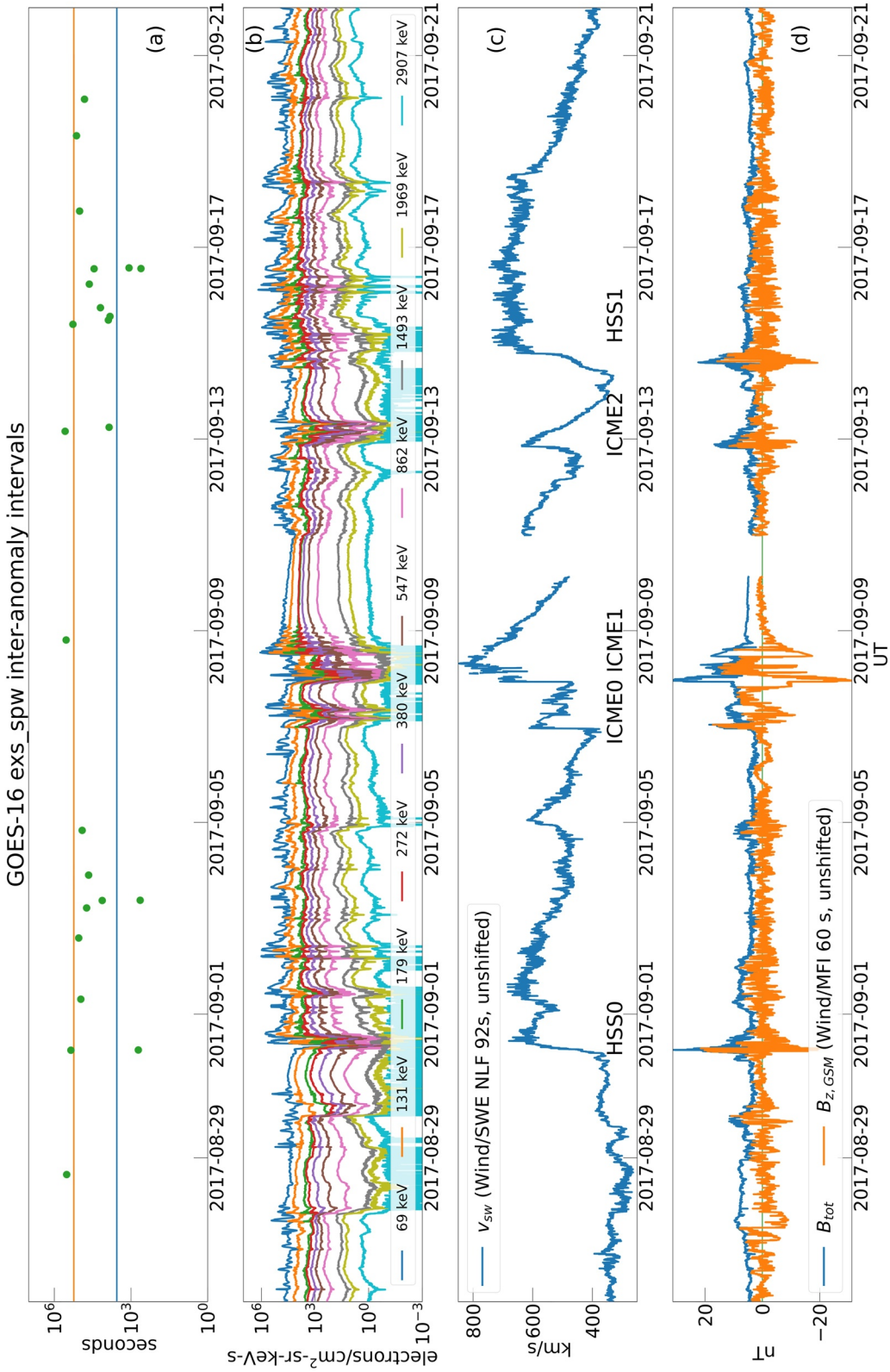

Figure 7. GOES-16 EXS_SPW anomalies, GOES-16 electron fluxes, and Wind solar wind velocity and magnetic field during Bartels Rotation 2511, 26 August–21 September 2017. (a) Inter-anomaly intervals, with horizontal lines at 1 hr and 2 days, (b) GOES-16 MPS-HI Telescope 4 5-min-averaged 69 keV–2.9 MeV electron fluxes, (c) Wind solar wind speed from non-linear fits, 92-s resolution, and (d) Wind magnetic field magnitude and GSM B_z component. The event labels on panel (c) are based on Redmon et al. (2018). The data gap on 10 September is from 0256 to 2350 UT and thus its relationship to the energetic solar energetic particle event that started at 1618 UT (Redmon et al., 2018) is unclear.

et al., 1993; Thomsen et al., 2013). As with the overall anomaly distribution (Kress et al., 2024), the magnetic local time (MLT) distributions of clustered anomalies have prominent pre-noon peaks, while the MLT distributions of background anomalies are statistically uniform (Figure 3). The number of clustered anomalies varies much more between Bartels solar rotation periods (BR) than the number of background anomalies. The MLT and BR variations of the clustered anomalies suggest that the internal charge accumulation (Bodeau, 2010; Romero & Levy, 1993) leading to the clustered anomalies has a time constant that is shorter than a day. The more uniform MLT distribution of the background anomalies and the comparative persistence of their rate between BRs (Figure 5) suggest that the charge accumulation leading to the background anomalies has a time constant of order one BR or longer. That is, there may be two distinct charging susceptibilities contributing to the observed EXS_SPW anomaly time series, involving different electrical time constants and possibly different energies. At 131 keV, the range of electrons in aluminum is 0.0076 cm or 3.0 mil (Tabata et al., 1972). This is much thinner than the shielding thickness capable of adequately reducing charge deposition by MeV electrons in GEO (NASA, 2017) (the range of 1 MeV electrons in aluminum is 0.15 cm or 58 mil (Tabata et al., 1972)). One possible scenario is that the 100–300 keV electrons are accumulating in a thinly shielded dielectric with a short (<1 day) electrical time constant, while MeV electrons are penetrating thicker shielding elsewhere and accumulating in a dielectric with an electrical time constant of order of the 27-day solar rotation period. The discharges due to both susceptibilities are coupling to the same cable and causing the same type of anomaly.

Even longer electrical time constants are realistic in contemporary spacecraft materials (Bodeau, 2010), and anomalies correlated with multi-day fluences of >2 MeV electrons have resulted from charge accumulation in such materials (Balcewicz et al., 2000; Bodeau, 2010; Lohmeyer et al., 2015). In contrast, the SCATHA anomalies attributed to internal charging, possibly of cables, had a local time (LT) distribution peaked near noon, which followed the local-time distribution of >300 keV electron fluxes in a near-geosynchronous orbit (Fennell et al., 2001; Koons, 1983; Koons et al., 2000; Koons & Gorney, 1991). They were also more likely to occur when Kp was greater than 4 (Koons & Gorney, 1991). These sensitivities to LT and Kp may indicate a short electrical time constant in the component being charged.

4.2. Distinguishing Clustered and Background Anomalies

As described in Section 3.2, an anomaly was identified as part of a cluster if it was preceded by or followed by an inter-anomaly interval shorter than 2 days. The complementary set constituted the background anomalies. The use of this criterion to automatically distinguish clustered and background anomalies resulted in distinct distributions for the two groups. The distributions for the clustered anomalies were peaked prior to noon and increased with *Kp*, while the distributions for the background anomalies were uniform in MLT and independent of *Kp*. Also, the number of clustered anomalies was greater than the number of background anomalies by a factor of $\sim$8. The simpler criterion, of using just the inter-anomaly interval preceding each anomaly to distinguish the two groups, resulted in more than twice the number of "background" anomalies, which exhibited a peak in the MLT distribution prior to noon (though statistically much more uniform than the clustered anomalies) and a *Kp* dependence. This sensitivity to the criterion used is a consequence of the ambiguity identified earlier. If in fact there are two charging mechanisms at work, then neither criterion is able to perfectly distinguish the two categories. Either choice causes contamination of one category. The criterion that uses only the preceding inter-anomaly intervals includes some "clustered" anomalies in the "background" category. Since the "clustered" distribution is much larger, the contamination level in the "background" category is large. This makes a truly uniform "background" distribution look non-uniform in MLT and *Kp*. The criterion using both the preceding and following inter-anomaly intervals (used in Section 3.2) includes some "background" anomalies in the "clustered" category. The contamination level is small, and the distribution of the "clustered" distribution is not altered qualitatively by the addition of a small, uniform distribution. In this way, the criterion used in Section 3.2 results in a better qualitative representation of the clustered and background distributions, although the background anomaly rate is probably underestimated. This ambiguity highlights the importance of having observations of radio bursts from ESD to help distinguish different ESD types, as on SCATHA (Koons et al., 2000; Koons & Gorney, 1991).

4.3. Are the Fluxes Associated With Anomaly Clusters Extreme?

Kress et al. (2024) found that the distributions of fluxes associated with the anomalies were significantly elevated with respect to the full distributions, according to three statistical measures. To quote one of these measures, the energies at which the median of the anomaly associated distribution was greater than the 75th percentile of the full

distribution in the near-equatorial look direction ranged from 18.3 to 860 keV, with the 100–300 keV fluxes being most elevated. The medians of the 131 keV distributions were the 85th and 87th percentiles of the full GOES-16 and -17 distributions, respectively. Some of the inter-anomaly intervals are quite short, suggesting intense internal charging current densities. An important question is how these elevated fluxes compare to historical extremes.

The SCATHA 24 April 1979 "worst-case" electron spectrum associated with severe spacecraft frame charging in sunlight (Gussenhoven & Mullen, 1983; Mullen et al., 1986) was "the most severe charging event encountered by the SCATHA satellite prior to September 22, 1982," when the largest discharges and the largest differential potentials since launch were observed (Koons et al., 1988). The "worst-case" electron spectrum of 22 September 1982 (Fennell et al., 2001; Koons et al., 1988; Roeder, 1994) exceeded the earlier spectrum (Gussenhoven & Mullen, 1983; Matéo-Vélez et al., 2018) below 6 keV and above 40 keV. In three high-level charging events, including the 24 April 1979 case, the 30–75 keV electron flux was most highly correlated with frame potential, while the correlation of >100 keV fluxes with frame potential ranged from anticorrelated to uncorrelated to highly correlated (Mullen et al., 1986). This result suggests that >100 keV fluxes are not reliably associated with frame potential. In contrast, these two "worst-case" spectra bracket electron flux increases at 288 keV associated with internal discharges on SCATHA (Koons & Gorney, 1991). Most of the fluxes associated with these internal discharges were bounded by the values of the two "worst-case" spectra at 288 keV (3.6×10^3 to 1.8×10^4 e/cm^2-s-sr-keV) (Matéo-Vélez et al., 2018; Roeder, 1994).

These spectra were identified as "worst-case" based on their charging effects on SCATHA, not in terms of their differential flux values. It is noteworthy, however, that the maximum 131, 179 and 272 keV electron fluxes observed during the study period approach the greater of these two "worst-case" spectra, from 22 September 1982 (Figure 8). Keeping in mind that SCATHA and GOES-16 and -17 have not been cross-calibrated, these comparisons show that the 22 September 1982 SCATHA "worst-case" fluxes in the 100–300 keV range are similar to the greatest flux levels in GEO associated with shallow internal charging on GOES-16 and -17. An important question is whether these flux levels represent true extremes, that is, natural limits to 100–300 keV fluxes in geostationary orbit. Through extreme value analysis of Los Alamos observations in GEO, O'Brien et al. (2007) determined that 270 keV electron fluxes have an upper limit of 1.5 to 2.6×10^4 e/cm^2-s-sr-keV (95% confidence interval), in good agreement with the "worst-case" SCATHA values and the greatest MPS-HI fluxes at this energy. The GOES 131 and 179 keV fluxes should be analyzed similarly, keeping in mind that several more years of data are needed to have a full solar cycle of MPS-HI fluxes.

5. Summary

In extending the work of Kress et al. (2024), this paper has determined the variation in the EXS_SPW anomaly occurrence rate over the study period (2017–2021), has identified the solar wind drivers with which the anomalies are associated, and from this has derived further insight into the nature of the anomalies themselves. The anomalies come in clusters, sometimes with clear 27-day periodicities, that have inter-anomaly intervals between <1 min and 2 days, in the presence of a background of anomalies that have longer inter-anomaly intervals. Anomaly clusters generally appear at both GOES-16 and GOES-17, although the actual anomaly times are different. The EXS_SPW anomalies are more likely to occur during high-speed solar wind streams (HSS) than not. In a superposed epoch analysis, during the 12 hr prior to clustered anomalies, the solar wind speed is greater and the number density is lower on average than prior to background anomalies. These periods are characterized by Alfvénic fluctuations in interplanetary magnetic field (IMF) B_z, and B_z is on average weakly negative in the 12 hr prior to these anomalies. The solar wind of the declining phase of a solar cycle and through solar minimum is characterized by such HSS originating in coronal holes, often recurring.

The study period, which spanned solar minimum, did not permit a comprehensive study of the effectiveness of interplanetary coronal mass ejections (ICMEs) in causing these anomalies. The fastest ICME during this period was relatively ineffective owing to its IMF rotating rapidly from a southward to a radial orientation. However, the time variation of the magnetic field in ICMEs varies markedly from event to event (Richardson & Cane, 2010). A continuation of this study through solar maximum would permit a study of the occurrence of these anomalies during a large number of ICMEs. Regardless, comparisons with published spectra (Gussenhoven & Mullen, 1983; O'Brien et al., 2007; Roeder, 1994) show that the extremes of 100–300 keV electron fluxes at GEO observed during the cycle 24/25 solar minimum, following the mildest cycle during the last 100 years, are comparable to

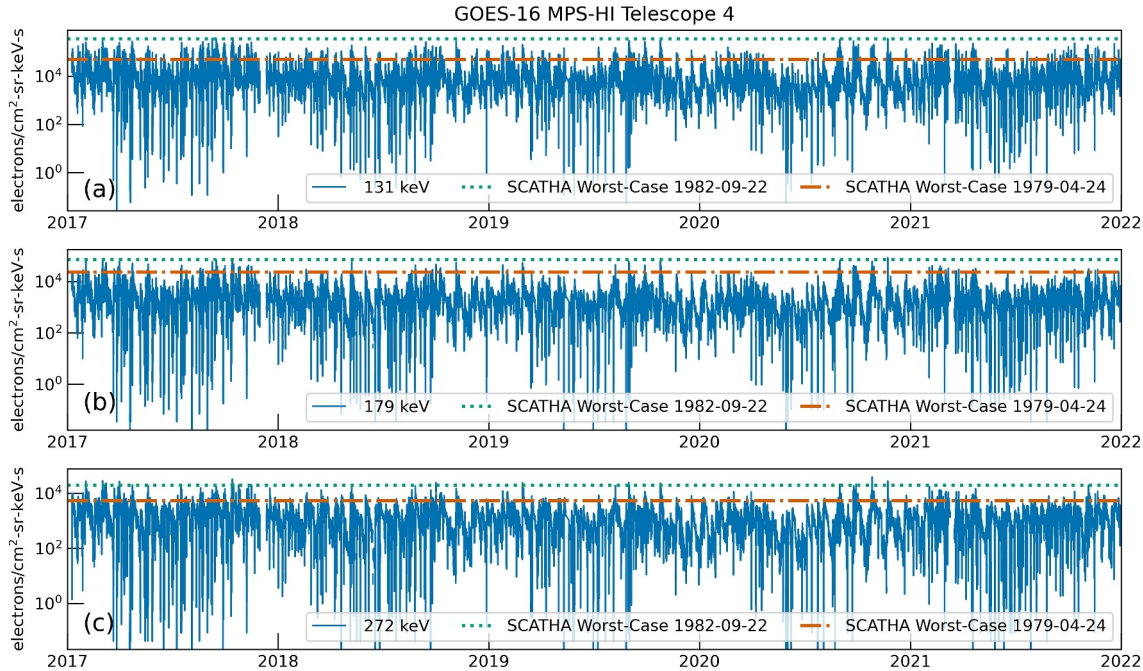

Figure 8. Plot of GOES-16 5-min-averaged radiation belt electron fluxes near 90° pitch angle, January 2017 – December 2021, along with levels from the SCATHA "worst case" electron spectra from 24 April 1979 (Gussenhoven & Mullen, 1983), using the three-Maxwellian fit by Matéo-Vélez et al. (2018), and from 22 September 1982 (Fennell et al., 2001; Koons et al., 1988; Roeder, 1994). (a) 131 keV, (b) 179 keV, (c) 272 keV.

"worst-case" spectra observed by SCATHA near the peak and during the declining phase of the intense solar cycle 21 and to an extreme value derived from observations during the intense cycles 22 and 23.

The shallow internal charging energy range studied here (100–300 keV) should be investigated further to understand the materials and configurations that are susceptible to such elevated electron spectra and whether existing design guidelines need to be revised in order to protect better against the charging effects of such spectra. Three-dimensional modeling and testing of the Space Wire cable are needed, guided by an assessment of the full electron spectra associated with these GOES anomalies, including the plasma below 50 keV (Kress et al., 2024). The shallow charging energy range coincides with the transition region between convection-dominated and radial diffusion-dominated transport, currently an area of active research (Ganushkina et al., 2015). Finally, this work and that of Kress et al. (2024) demonstrate the importance of having comprehensive spacecraft anomaly data available for studies in which good statistics can support accurate attribution of specific anomalies to the space environment and the development of anomaly models (Mazur & O'Brien, 2012; Thomsen et al., 2013).

Data Availability Statement

The GOES-16 and -17 MPS-HI radiation belt electron fluxes are available from the NOAA National Centers for Environmental Information (NCEI) (NOAA, 2024b). The GOES-16 and GOES-17 EXS_SPW anomaly lists for this study period (Kress et al., 2024) are available from NCEI (NOAA, 2024a). The *Kp* indices were downloaded from the Deutsches GeoForschungsZentrum GFZ (Matzka, Bronkalla, et al., 2021). We acknowledge use of NASA/GSFC's Space Physics Data Facility's OMNIWeb service, and OMNI data (Papitashvili & King, 2020a, 2020b). The Wind MFI data (WI_H0_MFI (Koval et al., 2021)) and SWE non-linear fit data (WI_H1_SWE (Ogilvie et al., 2021),) are from CDAWeb. The satellite magnetic local times were accessed from the NASA/GSFC Satellite Situation Center Web (SSCWeb) service (https://sscweb.gsfc.nasa.gov). The list of Bartels solar rotation numbers and periods was accessed at the ACE Science Center (ASC, 2023). This work utilises the HSS catalog issued by Mariş Muntean et al. (n.d.), managed by the Institute of Geodynamics of the Romanian Academy, and the list of near-earth ICMEs created by Richardson and Cane (2024).

Acknowledgments
This work was supported by NASA Living with a Star Grants 80NSSC19K0085 and NNG19OB09A. Support was also provided by the GOES-R program and the National Centers for Environmental Information (NCEI) through NOAA Cooperative Agreements NA22OAR4320151 and NA17OAR4320101. We thank R. Meloy and D. Pitchford for helpful discussions, and J. Spann and T. Leonard for reviewing an earlier version of this paper. The statements, findings, conclusions, and recommendations are those of the authors and do not necessarily reflect the views of NOAA or the U.S. Department of Commerce.

References

Alken, P., Thébault, E., Beggan, C. D., Amit, H., Aubert, J., Baerenzung, J., et al. (2021). International Geomagnetic Reference Field: The thirteenth generation. *Earth Planets and Space*, *73*, 1–25. https://doi.org/10.1186/s40623-020-01288-x

ASC. (2023). Bartels rotation numbers and dates for years 2004–2023 [Dataset]. *ACE Science Center, Caltech*. Retrieved from https://izw1.caltech.edu/ACE/ASC/DATA/bartels/Bartels2004-2023.pdf

Balcewicz, P. T., Bodeau, J. M., Frey, M. A., Leung, P. L., & Mikkelson, E. J. (2000). Environmental on-orbit anomaly correlation efforts at Hughes. In *Proceedings of the 6th Spacecraft Charging Technology Conference* (pp. 227–230). Retrieved from https://www.spis.org/archives/projects/spine/home/tools/sctc/VIth/78be82b6c0a800140147686b26901281/6th_Environmental_On-Orbit_Anomaly_Correlation_Efforts_51.pdf

Bartels, J. (1934). Twenty-seven day recurrences in terrestrial-magnetic and solar activity, 1923–1933. *Terrestrial Magnetism and Atmospheric Electricity*, *39*(3), 201–202a. https://doi.org/10.1029/TE039i003p00201

Baumjohann, W. (1986). Merits and limitations of the use of geomagnetic indices in solar wind-magnetosphere coupling studies. In Y. Kamide & J. A. Slavin (Eds.), *Solar wind-magnetosphere coupling* (pp. 3–15). Terra Scientific.

Belcher, J. W., & Davis, L. Jr. (1971). Large-amplitude Alfvén waves in the interplanetary medium, 2. *Journal of Geophysical Research (1896–1977)*, *76*(16), 3534–3563. https://doi.org/10.1029/JA076i016p03534

Besliu-Ionescu, D., Maris Muntean, G., & Dobrica, V. (2022). Complex catalogue of high speed streams associated with geomagnetic storms during Solar Cycle 24. *Solar Physics*, *297*(5), 65. https://doi.org/10.1007/s11207-022-01998-3

Bodeau, M. (2010). High energy electron climatology that supports deep charging risk assessment in GEO. In *48th AIAA Aerospace Sciences Meeting* (p. 1608). https://doi.org/10.2514/6.2010-1608

Boudouridis, A., Rodriguez, J. V., Kress, B. T., Dichter, B. K., & Onsager, T. G. (2020). Development of a bowtie inversion technique for real-time processing of the GOES-16/-17 SEISS MPS-HI electron channels. *Space Weather*, *18*(4), e2019SW002403. https://doi.org/10.1029/2019SW002403

Burlaga, L. F. (1974). Interplanetary stream interfaces. *Journal of Geophysical Research (1896–1977)*, *79*(25), 3717–3725. https://doi.org/10.1029/JA079i025p03717

DeForest, S. E. (1972). Spacecraft charging at synchronous orbit. *Journal of Geophysical Research*, *77*(4), 651–659. https://doi.org/10.1029/JA077i004p00651

Denton, M. H., & Borovsky, J. E. (2012). Magnetosphere response to high-speed solar wind streams: A comparison of weak and strong driving and the importance of extended periods of fast solar wind. *Journal of Geophysical Research*, *117*(A9). https://doi.org/10.1029/2011JA017124

Dichter, B. K., Galica, G. E., McGarity, J. O., Tsui, S., Golightly, M. J., Lopate, C., & Connell, J. J. (2015). Specification, design, and calibration of the space weather suite of instruments on the NOAA GOES-R program spacecraft. *IEEE Transactions on Nuclear Science*, *62*(6), 2776–2783. https://doi.org/10.1109/TNS.2015.2477997

Farthing, W., Brown, J., & Bryant, W. (1982). *Differential spacecraft charging on the geostationary operational environmental satellites (Tech. Rep. No. TM 83908)*. NASA. Retrieved from https://ntrs.nasa.gov/citations/19820018480

Fennell, J. F., Koons, H., Roeder, J., & Blake, J. (2001). *Spacecraft charging: Observations and relationship to satellite anomalies (Tech. Rep. No. TR-2001(8570)-5)*. The Aerospace Corporation. Retrieved from https://apps.dtic.mil/sti/pdfs/ADA394826.pdf

Ferguson, D. C., Denig, W. F., & Rodriguez, J. V. (2011). Plasma conditions during the Galaxy 15 anomaly and the possibility of ESD from subsurface charging. In *49th AIAA Aerospace Sciences Meeting including the New Horizons Forum and Aerospace Exposition*. (AIAA 2011–1061). https://doi.org/10.2514/6.2011-1061

Ganushkina, N. Y., Amariutei, O. A., Welling, D., & Heynderickx, D. (2015). Nowcast model for low-energy electrons in the inner magnetosphere. *Space Weather*, *13*(1), 16–34. https://doi.org/10.1002/2014SW001098

Ganushkina, N. Y., Sillanpää, I., Welling, D., Haiducek, J., Liemohn, M., Dubyagin, S., & Rodriguez, J. V. (2019). Validation of Inner Magnetosphere Particle Transport and Acceleration Model (IMPTAM) with long-term GOES MAGED measurements of KEV electron fluxes at geostationary orbit. *Space Weather*, *17*(5), 687–708. https://doi.org/10.1029/2018SW002028

Ganushkina, N. Y., Swiger, B., Dubyagin, S., Matéo-Vélez, J.-C., Liemohn, M. W., Sicard, A., & Payan, D. (2021). Worst-case severe environments for surface charging observed at LANL satellites as dependent on solar wind and geomagnetic conditions. *Space Weather*, *19*(9), e2021SW002732. https://doi.org/10.1029/2021SW002732

Garrett, H. B. (1981). The charging of spacecraft surfaces. *Reviews of Geophysics*, *19*(4), 577–616. https://doi.org/10.1029/RG019i004p00577

Green, J. C., Likar, J., & Shprits, Y. (2017). Impact of space weather on the satellite industry. *Space Weather*, *15*(6), 804–818. https://doi.org/10.1002/2017SW001646

Gussenhoven, M. S., & Mullen, E. G. (1983). Geosynchronous environment for severe spacecraft charging. *Journal of Spacecraft and Rockets*, *20*(1), 26–34. https://doi.org/10.2514/3.28353

Hsu, T.-S., & McPherron, R. L. (2003). Occurrence frequencies of IMF triggered and nontriggered substorms. *Journal of Geophysical Research*, *108*(A7), 1307. https://doi.org/10.1029/2002JA009442

Jaynes, A. N., Baker, D. N., Singer, H. J., Rodriguez, J. V., Loto'aniu, T. M., Ali, A. F., et al. (2015). Source and seed populations for relativistic electrons: Their roles in radiation belt changes. *Journal of Geophysical Research: Space Physics*, *120*(9), 7240–7254. https://doi.org/10.1002/2015JA021234

Kasper, J. C., Lazarus, A. J., Steinberg, J. T., Ogilvie, K. W., & Szabo, A. (2006). Physics-based tests to identify the accuracy of solar wind ion measurements: A case study with the Wind Faraday Cups. *Journal of Geophysical Research*, *111*(A3). https://doi.org/10.1029/2005JA011442

King, J. H., & Papitashvili, N. E. (2005). Solar wind spatial scales in and comparisons of hourly Wind and ACE plasma and magnetic field data. *Journal of Geophysical Research*, *110*(A2). https://doi.org/10.1029/2004JA010649

Koons, H. C. (1983). Summary of Environmentally Induced Electrical Discharges on the P78-2 (SCATHA) satellite. *Journal of Spacecraft and Rockets*, *20*(5), 425–431. https://doi.org/10.2514/3.25623

Koons, H. C., Fennell, J. F., & Hall, D. F. (2000). A summary of the engineering results from the Aerospace Corporation experiments on the SCATHA spacecraft. In *Proceedings of the 6th Spacecraft Charging Technology Conference* (pp. 243–249). Retrieved from https://www.spis.org/archives/projects/spine/home/tools/sctc/VIth/78bb0050c0a800140003d22eb8bb547e/6th_A_Summary_of_the_Engineering_Results_from_the_Aero_54.pdf

Koons, H. C., & Gorney, D. J. (1991). Relationship between electrostatic discharges on spacecraft P78-2 and the electron environment. *Journal of Spacecraft and Rockets*, *28*(6), 683–688. https://doi.org/10.2514/3.26300

Koons, H. C., Mizera, P. F., Roeder, J. L., & Fennell, J. F. (1988). Several spacecraft-charging event on SCATHA in September 1982. *Journal of Spacecraft and Rockets*, *25*(3), 239–243. https://doi.org/10.2514/3.25977

Korth, H., Thomsen, M. F., Borovsky, J. E., & McComas, D. J. (1999). Plasma sheet access to geosynchronous orbit. *Journal of Geophysical Research*, *104*(A11), 25047–25061. https://doi.org/10.1029/1999JA900292

Koval, A., Lepping, R. P., & Szabo, A. (2021). Wind Magnetic Field Investigation (MFI) composite data (WI_H0_MFI) [Dataset]. *NASA Space Physics Data Facility*. https://doi.org/10.48322/av38-wn55

Krause, L. H., Dichter, B. K., Knipp, D. J., & Ray, K. P. (2000). The relationship between DSCS III sunlit surface charging and geomagnetic activity indices. *IEEE Transactions on Nuclear Science*, *47*(6), 2224–2230. https://doi.org/10.1109/23.903757

Kress, B. T., Rodriguez, J. V., Buzulukova, N. Y., Redmon, R. J., Machol, J. L., Fiorello, J. L., et al. (2024). Relationship between GOES-R series spacecraft operational anomalies and in-situ 30 eV–3 MeV electron measurements. *IEEE Transactions on Plasma Science*, *52*(5), 1610–1618. https://doi.org/10.1109/TPS.2024.3390658

Lee, D.-Y., Lyons, L. R., Kim, K. C., Baek, J.-H., Kim, K.-H., Kim, H.-J., et al. (2006). Repetitive Substorms caused by Alfvénic waves of the interplanetary magnetic field during high-speed solar wind streams. *Journal of Geophysical Research*, *111*(A12). https://doi.org/10.1029/2006JA011685

Lepping, R., Acuña, M., Burlaga, L., Farrell, W., Slavin, J., Schatten, K., et al. (1995). The Wind magnetic field investigation. *Space Science Reviews*, *71*(1–4), 207–229. https://doi.org/10.1007/BF00751330

Lindblad, B., & Lundstedt, H. (1981). A catalogue of high-speed plasma streams in the solar wind. *Solar Physics*, *74*(1), 197–206. https://doi.org/10.1007/BF00151290

Lohmeyer, W., & Cahoy, K. (2013). Space weather radiation effects on geostationary satellite solid-state power amplifiers. *Space Weather*, *11*(8), 476–488. https://doi.org/10.1002/swe.20071

Lohmeyer, W., Carlton, A., Wong, F., Bodeau, M., Kennedy, A., & Cahoy, K. (2015). Response of geostationary communications satellite solid-state power amplifiers to high-energy electron Fluence. *Space Weather*, *13*(5), 298–315. https://doi.org/10.1002/2014SW001147

Loto'aniu, T. M., Singer, H. J., Rodriguez, J. V., Green, J., Denig, W., Biesecker, D., & Angelopoulos, V. (2015). Space weather conditions during the Galaxy 15 spacecraft anomaly. *Space Weather*, *13*(8), 484–502. https://doi.org/10.1002/2015SW001239

Loto'aniu, T. M., Singer, H. J., Waters, C. L., Angelopoulos, V., Mann, I. R., Elkington, S. R., & Bonnell, J. W. (2010). Relativistic electron loss due to ultralow frequency waves and enhanced outward radial diffusion. *Journal of Geophysical Research*, *115*(A12). https://doi.org/10.1029/2010JA015755

Mariş Muntean, G., Beşliu-Ionescu, D., & Dobrică, V. (n.d.). Complex catalogue of high speed streams and geomagnetic storms during solar cycle 24 [Dataset]. *Romanian Academy Institute of Geodynamics Sabba S. Ştefănescu*. Retrieved from https://www.geodin.ro/varsiti/

Matéo-Vélez, J.-C., Sicard, A., Payan, D., Ganushkina, N., Meredith, N. P., & Sillanpää, I. (2018). Spacecraft surface charging induced by severe environments at geosynchronous orbit. *Space Weather*, *16*(1), 89–106. https://doi.org/10.1002/2017SW001689

Matzka, J., Bronkalla, O., Tornow, K., Elger, K., & Stolle, C. (2021a). Geomagnetic Kp index. v.1.0 [Dataset]. *GFZ Data Services*. https://doi.org/10.5880/Kp.0001

Matzka, J., Stolle, C., Yamazaki, Y., Bronkalla, O., & Morschhauser, A. (2021b). The geomagnetic *Kp* index and derived indices of geomagnetic activity. *Space Weather*, *19*(5), e2020SW002641. https://doi.org/10.1029/2020SW002641

Mazur, J. E., & O'Brien, T. P. (2012). Comment on "Analysis of GEO spacecraft anomalies: Space weather relationships" by Ho-Sung Choi et al. *Space Weather*, *10*(3). https://doi.org/10.1029/2011SW000738

McPherron, R. L., & Manka, R. H. (1985). Dynamics of the 1054 UT march 22, 1979, substorm event: CDAW 6. *Journal of Geophysical Research*, *90*(A2), 1175–1190. https://doi.org/10.1029/JA090iA02p01175

Minow, J. I., Jordanova, V. K., Pitchford, D., Ganushkina, N. Y., Zheng, Y., Delzanno, G., et al. (2024). ISWAT spacecraft surface charging review. *Advances in Space Research*. https://doi.org/10.1016/j.asr.2024.08.058

Miyoshi, Y., & Kataoka, R. (2008). Flux enhancement of the outer radiation belt electrons after the arrival of stream interaction regions. *Journal of Geophysical Research*, *113*(A3), A03S09. https://doi.org/10.1029/2007JA012506

Mullen, E. G., Gussenhoven, M. S., Hardy, D. A., Aggson, T. A., Ledley, B. G., & Whipple, E. (1986). SCATHA survey of high-level spacecraft charging in sunlight. *Journal of Geophysical Research*, *91*(A2), 1474–1490. https://doi.org/10.1029/JA091iA02p01474

Nagai, T., Shinohara, I., Singer, H. J., Rodriguez, J., & Onsager, T. G. (2019). Proton and electron injection path at geosynchronous altitude. *Journal of Geophysical Research: Space Physics*, *124*(6), 4083–4103. https://doi.org/10.1029/2018JA026281

NASA. (2017). *Mitigating in-space charging effects–a guideline (Tech. Rep. No. NASA-HDBK-4002A with Change 1)*. National Aeronautics and Space Administration.

Neugebauer, M., Goldstein, R., & Goldstein, B. E. (1997). Features observed in the trailing regions of interplanetary clouds from coronal mass ejections. *Journal of Geophysical Research*, *102*(A9), 19743–19751. https://doi.org/10.1029/97JA01651

NOAA. (2024a). GOES-16 and GOES-17 EXIS space Wire anomalies [Dataset]. *NOAA National Centers for Environmental Information*. Retrieved from https://www.ncei.noaa.gov/products/satellite-anomalies

NOAA. (2024b). GOES-R Space Environment In Situ Suite (SEISS) [Dataset]. *NOAA National Centers for Environmental Information*. Retrieved from https://www.ncei.noaa.gov/products/goes-r-space-environment-in-situ

O'Brien, T. P. (2009). SEAES-GEO: A spacecraft environmental anomalies expert system for geosynchronous orbit. *Space Weather*, *7*(9). https://doi.org/10.1029/2009SW000473

O'Brien, T. P., Fennell, J. F., Roeder, J. L., & Reeves, G. D. (2007). Extreme electron fluxes in the outer zone. *Space Weather*, *5*(1). https://doi.org/10.1029/2006SW000240

Ogilvie, K. W., Fitzenreiter, R. J., Lazarus, A. J., Kasper, J. C., & Stevens, M. L. (2021). Wind Solar Wind Experiment (SWE) 92-sec definitive solar wind proton data (WI_H1_SWE) [Dataset]. *NASA Space Physics Data Facility*. https://doi.org/10.48322/nasd-j276

Onsager, T. G., Grubb, R., Kunches, J., Matheson, L., Speich, D., Zwickl, R. W., & Sauer, H. (1996). Operational uses of the GOES energetic particle detectors. In E. R. Washwell (Ed.), *GOES-8 and beyond* (Vol. 2812, pp. 281–290). SPIE. https://doi.org/10.1117/12.254075

Onsager, T. G., Rostoker, G., Kim, H.-J., Reeves, G. D., Obara, T., Singer, H. J., & Smithtro, C. (2002). Radiation belt electron flux dropouts: Local time, radial, and particle-energy dependence. *Journal of Geophysical Research*, *107*(A11), SMP21. https://doi.org/10.1029/2001JA000187

Ozkul, A., Lopatin, A., Shipp, A., Pitchford, D., Mazur, J. E., Roeder, J. L., et al. (2001). *Initial correlation results of charge sensor data from six INTELSAT VIII class satellites with other space and ground based measurements* (Vol. ESA-SP-476, pp. 293–298). European Space Agency Publications. Retrieved from https://www.spis.org/archives/projects/spine/home/tools/sctc/VIIth/791fefe8c0a800140109ac5fca48f9c0/7th_Initial_Correlation_Results_of_Charge_Sensor_Data__51.pdf

Papitashvili, N. E., & King, J. H. (2020a). OMNI 1-min data set [Dataset]. *NASA Space Physics Data Facility*. https://doi.org/10.48322/45bb-8792

Papitashvili, N. E., & King, J. H. (2020b). OMNI hourly data [Dataset]. *NASA Space Physics Data Facility*. https://doi.org/10.48322/1shr-ht18

Paulikas, G., & Blake, J. (1979). Effects of the solar wind on magnetospheric dynamics: Energetic electrons at the synchronous orbit. In *Quantitative modeling of magnetospheric processes* (pp. 180–202). American Geophysical Union (AGU). https://doi.org/10.1029/GM021p0180

Press, W. H., Flannery, B. P., Teukolsky, S. A., & Vetterling, W. T. (1988). *Numerical recipes in C*. Cambridge University Press.

Redmon, R. J., Seaton, D. B., Steenburgh, R., He, J., & Rodriguez, J. V. (2018). 2017's geoeffective space weather and impacts to Caribbean radio communications during hurricane response. *Space Weather*, *16*(9), 1190–1201. https://doi.org/10.1029/2018SW001897

Richardson, I. G., & Cane, H. V. (2010). Near-earth interplanetary coronal mass ejections during solar cycle 23 (1996–2009): Catalog and summary of properties. *Solar Physics*, *264*(1), 189–237. https://doi.org/10.1007/s11207-010-9568-6

Richardson, I. G., & Cane, H. V. (2024). Near-earth interplanetary coronal mass ejections since January 1996 [Dataset]. *NASA Goddard Space Flight Center, University of Maryland, College Park, and University of Tasmania*. https://doi.org/10.7910/DVN/C2MHTH

Roeder, J. (1994). *Specification of the plasma environment at geosynchronous orbit in the energy range 87 eV to 288 keV (Tech. Rep. No. TR-94 (4940)-6)*. The Aerospace Corporation. Retrieved from https://apps.dtic.mil/sti/tr/pdf/ADA308110.pdf

Romero, M., & Levy, L. (1993). Internal charging and secondary effects. In R. N. DeWitt, D. Duston, & A. K. Hyder (Eds.), *The behavior of systems in the space environment* (pp. 565–580). Springer. https://doi.org/10.1007/978-94-011-2048-7_23

Russell, C. T. (1971). Geophysical coordinate transformations. *Cosmic Electrodynamics*, *2*(2), 184–196.

Schrijver, C. J. (2015). Socio-economic hazards and impacts of space weather: The important range between mild and extreme. *Space Weather*, *13*(9), 524–528. https://doi.org/10.1002/2015SW001252

Spence, H. E., Blake, J. B., & Fennell, J. F. (1993). Surface charging analysis of high-inclination, high-altitude spacecraft: Identification and physics of the plasma source region. *IEEE Transactions on Nuclear Science*, *40*(6), 1521–1524. https://doi.org/10.1109/23.273510

Tabata, T., Ito, R., & Okabe, S. (1972). Generalized semiempirical equations for the extrapolated range of electrons. *Nuclear Instruments and Methods*, *103*(1), 85–91. https://doi.org/10.1016/0029-554X(72)90463-6

Thomsen, M. F. (2004). Why Kp is such a good measure of magnetospheric convection. *Space Weather*, *2*(11). https://doi.org/10.1029/2004SW000089

Thomsen, M. F., Henderson, M. G., & Jordanova, V. K. (2013). Statistical properties of the surface-charging environment at geosynchronous orbit. *Space Weather*, *11*(5), 237–244. https://doi.org/10.1002/swe.20049

Thomsen, M. F., McComas, D. J., Borovsky, J. E., & Elphic, R. C. (1998). The magnetospheric trough. In J. L. Horwitz, D. L. Gallagher, & W. K. Peterson (Eds.), *Geospace mass and energy flow, Geophysical Monograph 104* (pp. 355–369). American Geophysical Union (AGU). https://doi.org/10.1029/GM104p0355

Tsurutani, B. T., Gonzalez, W. D., Gonzalez, A. L. C., Guarnieri, F. L., Gopalswamy, N., Grande, M., et al. (2006). Corotating solar wind streams and recurrent geomagnetic activity: A review. *Journal of Geophysical Research*, *111*(A7). https://doi.org/10.1029/2005JA011273

Vampola, A. L. (1987). Thick dielectric charging on high-altitude spacecraft. *Journal of Electrostatics*, *20*(1), 21–30. https://doi.org/10.1016/0304-3886(87)90083-0

Weygand, J. M., & McPherron, R. L. (2006). Dependence of ring current asymmetry on storm phase. *Journal of Geophysical Research*, *111*(A11), A11221. https://doi.org/10.1029/2006JA011808

Wilkinson, D. C. (1994). National Oceanic and Atmospheric Administration's spacecraft anomaly data base and examples of solar activity affecting spacecraft. *Journal of Spacecraft and Rockets*, *31*(2), 160–165. https://doi.org/10.2514/3.26417

Wrenn, G. L., & Smith, R. J. K. (1996). Probability factors governing ESD effects in geosynchronous orbit. *IEEE Transactions on Nuclear Science*, *43*(6), 2783–2789. https://doi.org/10.1109/23.556867